A&A 595, A79 (2016)
DOI: 10.1051/0004-6361/201628544

Astronomy & Astrophysics

High-contrast imaging of ϵ Eridani with ground-based instruments

T. Mizuki[1], T. Yamada[1,2], J. C. Carson[3], M. Kuzuhara[4,5], T. Nakagawa[2], J. Nishikawa[5,6], M. L. Sitko[7], T. Kudo[8], N. Kusakabe[5], J. Hashimoto[5], L. Abe[9], W. Brander[10], T. D. Brandt[11], S. Egner[8], M. Feldt[10], M. Goto[12], C. A. Grady[13,14,15], O. Guyon[8], Y. Hayano[8], M. Hayashi[6], S. S. Hayashi[8], T. Henning[10], K. W. Hodapp[16], M. Ishii[6], M. Iye[6], M. Janson[17], R. Kandori[6], G. R. Knapp[17], J. Kwon[2,6], T. Matsuo[19], M. W. McElwain[13], S. Miyama[20], J. Morino[6], A. Moro-Martin[17,21], T. Nishimura[8], T. Pyo[8], E. Serabyn[22], T. Suenaga[6,23], H. Suto[5,6], R. Suzuki[6], Y. H. Takahashi[6,18], M. Takami[24], N. Takato[8], H. Terada[6], C. Thalmann[25], E. L. Turner[17,26], M. Watanabe[27], J. Wisniewski[28], H. Takami[6], T. Usuda[6], and M. Tamura[5,6,18]

(Affiliations can be found after the references)

Received 18 March 2016 / Accepted 23 August 2016

ABSTRACT

ϵ Eridani is one of the nearest solar-type stars. Its proximity and relatively young age allow high-contrast imaging observations to achieve sensitivities to planets at narrow separations down to an inner radius of ~5 AU. Previous observational studies of the system report a dust disk with asymmetric morphology as well as a giant planet with large orbital eccentricity, which may require another massive companion to induce the peculiar morphology and to enhance the large orbital eccentricity. In this paper, we report results from deep high-contrast imaging observations to detect the previously reported planet and search for other unseen less massive companions with Subaru/HiCIAO, Gemini-South/NICI, and VLT/NACO. No positive detection was made, but high-contrast measurements with the CH_4S narrow-band filter of HiCIAO achieved sensitivities at 14.7 mag differential magnitude level, at an angular separation of 1.0″. In terms of planetary mass, as determined by cooling evolutionary models, the highest sensitivities were achieved by the Lp broad-band filter of NACO, resulting in sensitivities corresponding to 1.8, 2.8, and 4.5 $M_{\rm jup}$ at the projected separation of 3 AU, if 200, 400, and 800 Myr is assumed for the age of the system, respectively. We also discuss origins of the dust disk from the detection sensitivity in the planetary mass and find that a less massive eccentric planet is preferred for disk stirring, which is consistent with the orbital parameters of ϵ Eri b claimed from the previous long-term radial velocity monitoring.

Key words. planets and satellites: general – stars: individual: ϵ Eridani – instrumentation: adaptive optics – techniques: image processing

1. Introduction

Since the discovery of 51 Peg b (Mayor & Queloz 1995), more than 2000 exoplanets have been detected by various complementary methods (Extrasolar Planets Encyclopaedia[1]), allowing us to recognize the diversity of planetary systems in the Milky Way galaxy, and those discoveries of exoplanet have raised many open questions in understanding their formation and evolution processes. Very close stars are potentially very useful and are unique targets for detecting and characterizing exoplanets, especially those at small orbital radii from the host star, thanks to their natural accommodation of high spatial resolution imaging and to the large apparent luminosity of any potential exoplanets.

Among very nearby solar-type stars, ϵ Eri is one of the most interesting targets. For high-contrast imaging, the relatively young age of the system is essential in observing self-luminous low-mass objects. In addition, the star has both a massive planet and a dust disk at similar respective locations to that of Jupiter and the Kuiper belt in our own solar system, implying that a similar planet formation – an accretion-based planet formation that is widely accepted as the most likely planet formation model (e.g., Pollack et al. 1996; Ida & Lin 2004) – has occurred around ϵEri and the Sun. Long-term radial velocity (RV) monitoring has resulted in the discovery of a giant planet, ϵ Eri b, around the system (Hatzes et al. 2000). Sub-mm wavelength observations have revealed the presence of a spatially asymmetric dust-disk structure (Greaves et al. 1998). The RV-discovered planet, ϵ Eri b, has a relatively large orbital eccentricity, which may have resulted from interaction with other companions (e.g., Wu & Murray 2003; Ida et al. 2013). The asymmetric disk structure also suggests another massive planet at wide orbit, which may be necessary to explain the disk's morphology and dust replenishment.

We report here the results of direct imaging observations for ϵ Eri with several ground-based instruments[2], and achieve the highest contrast measurements for the star obtained so far. We also discuss the likely origins of observed features of the planetary system. The target properties are presented in Sect. 2. Observations and analysis are detailed in Sect. 3. Section 4 shows the observational results, along with the corresponding constraints such observations place on the planetary system. In Sect. 5, we summarize the current constraints for the system with the ground-based high-contrast imagings, and discuss the possible future observational approaches.

2. Properties of the ϵ Eri system

ϵ Eri is a K2V-type active star at a distance of 3.22 pc. Mamajek & Hillenbrand (2008) carried out a comprehensive study for the age of the star. Using chromospheric activities and the period of spin as age indicators, they found 400 Myr and 800 Myr for the age of the star, respectively. On the other hand,

[1] http://exoplanet.eu/

[2] In this work we use high-contrast imaging data of ϵ Eri obtained as a part of the SEEDS survey at the Subaru telescope, and archival data downloaded from the Gemini Science Archive and the ESO Archive.

Table 1. Stellar properties of ϵ Eri.

Property	
Name	ϵ Eri, GJ144, HIP16537
Coordinate (J2000)	03 32 55.84, –09 27 29.73[a]
Proper motion (mas/yr)	–975.17 ± 0.20, 19.49 ± 0.20[a]
Distance (pc)	3.218 ± 0.002[a]
Spectral type	K2V[b]
Temperature (K)	4999[b]
Surface gravity; log g	4.53[b]
Metallicity [Fe/H]	–0.1[b]
V-band mag (mag)	3.72[c]
R-band mag (mag)	3.00[c]
J-band mag (mag)	2.23[d]
H-band mag (mag)	1.88[d]
K-band mag (mag)	1.78[d]
Age (Myr)	200, 400, 800[e]

Notes. [(a)] Coodinates, proper motion, and parallax are taken from the HIPPARCOS catalogue (van Leeuwen 2007). [(b)] Spectral type, effective temperature, surface gravity, and metallicity are obtained via spectroscopy for dwarfs in the HIPPARCOS catalogue (Gray et al. 2006). [(c)] V- and R-band magnitudes taken from Tycho 1, 2 catalogues (Hoeg et al. 1997; Høg et al. 2000). [(d)] J-, H-, and K-band magnitudes taken from the 2MASS catalogue (Cutri et al. 2003) [(e)] System age of the target was obtained from Fuhrmann (2004), Mamajek & Hillenbrand (2008).

a younger age of 200 Myr is suggested from a pure kinematical analysis (Fuhrmann 2004). For the purposes of this paper, we consider the possible range to span from 200 to 800 Myr. The stellar properties of ϵ Eri are summarized in Table 1.

Previous observations at 850 μm with SCUBA at the JCMT successfully showed thermal emission from an asmymetric dust disk (Greaves et al. 1998). The asymmetric nature of the disk has also been confirmed via imaging at 160 μm, 450 μm, and 1.2 mm with the SCUBA and MAMBO at the IRAM 30-m telescope (Greaves et al. 2005; Lestrade & Thilliez 2015). In addition, the excess at far-infrared wavelengths observations by the *Spitzer* space telescope indicates the presence of asteroid populations with radii of 10 and 1 km at the inner and outer edge of the disk, respectively (Greaves et al. 2014). Since the lifetime of the circumstellar dust is shorter than the age of the host star because of dissipation due to radiation pressure and gravitational scattering effects, continuous replenishment of dust generated from asteroids in a collisional cascade must be considered (Wyatt 2008, and references therein). It is interesting to note that the observed dust disk of ϵ Eri has a clumpy morphology (Greaves et al. 1998, 2005; Lestrade & Thilliez 2015). To explain the asymmetric feature, planets around the star may be required.

A radial velocity curve indicating the presence of a giant planet with $M \sin i = 0.86\ M_{\rm jup}$ at 3.4 AU was previously reported (Hatzes et al. 2000). The orbital parameters and inferred physical properties of the giant planet have been updated in subsequent works using astrometry and cross-correlation re-analysis (e.g., Benedict et al. 2006; Anglada-Escudé & Butler 2012). The large orbital eccentricity of the giant planet – 0.4, 0.6, and 0.7 – were indicated in many of those studies. These orbital parameters are summarized in Table 2. The eccentric orbit of ϵ Eri b is indeed preferred to explain the presence of the replenished dust disk. It should be noted, however, that the orbital parameters of ϵ Eri b still need to be refined since there are large uncertainties in the RV measurement owing to the high activity of the host star.

Table 2. Orbital elements of ϵ Eri b.

Property	H00[a]	B06[b]	AB12[c]
$M_{\rm s}$ ($M_\odot$)	0.85	0.83	0.82
a (AU)	3.4	3.39 ± 0.36	3.51
P (year)	6.8 5± 0.06	6.85 ± 0.03	7.26
e	0.608 ± 0.041	0.702 ± 0.039	0.4
Ω (degree)	–	254	–
ω (degree)	48.9 ± 4.1	47	141.4
$M_{\rm p} \sin i$ ($M_{\rm jup}$)	0.86	0.78 ± 0.08	0.645
i (degree)	–	30.1 ± 3.8	–

Notes. Orbital parameters obtained in previous studies are presented. [(a)] Hatzes et al. (2000); [(b)] Benedict et al. (2006); [(c)] Anglada-Escudé & Butler (2012).

Furthermore, the presence of ϵ Eri b is still uncertain because Zechmeister et al. (2013) could not recover the planet even with the better precision in RV measurements. Complementary high-contrast imaging has been conducted with several different facilities, but no significant signals of companions around ϵ Eri have been reported so far (Janson et al. 2008; Heinze et al. 2010a,b; Janson et al. 2015).

3. Observation and analysis

We analyze here newly obtained data, as well as archival, high-contrast imaging data of ϵ Eri. Observing properties such as imaging mode, integration time, and rotation angle for each dataset are summarized in Table 3.

3.1. Subaru/HiCIAO $CH_4S + CH_4L$ narrow-band data

ϵ Eri was observed by HiCIAO at the Subaru Telescope on 5 September 2011 with the Spectral (Simultaneous) Differential Imaging and Angular Differential Imaging mode (Racine et al. 1999; Marois et al. 2006), using the narrow-band filters at H-band. The observations were conducted as a part of the Subaru SEEDS survey (Tamura 2009).

For the data reduction, we first corrected the stripe pattern in the HiCIAO raw image (Suzuki et al. 2010). The pattern has two components: 32 horizontal features correspond to different readout segments, and there are also 64 thin vertical stripe features. For each individual science frame, we measured and modeled these patterns using portions of the image separate from the host and free of celestial sources. The modeled patterns were then subtracted. For the de-striped frames, we then carried out deviant pixel correction and flat fielding. Reference frames without the saturation were taken just before and after the masked sequence, and the centroid of which were registered by the elliptical Gaussian fitting. The centroid shift on the detector in the masked sequence was predicted from a two-order polynomial fitting for reference centroids, and then adjusted.

The Spectral Differential Imaging mode of HiCIAO uses a Wollaston prism to simultaneously take images through different filters. For the case of HiCIAO's two-channel SDI mode, the two narrow-band filters, CH_4S (1.486–1.628 μm) and CH_4L (1.643–1.788 μm) were designed to obtain the flux difference of substellar companions caused by the band head of methane. Substellar objects like T-dwarfs show deep methane absorption (1.58–1.66 μm) in their cool atmospheric spectra (Burgasser et al. 2006, and references therein). The SDI mode allows the performance of effective PSF subtraction thanks to

Table 3. Observing properties of ϵ Eri.

Properties\Instrument	HiCIAO	NICI	NACO	NACO
Filter	$CH_4S + CH_4L$	$CH_4S + CH_4L(4\%)$	Lp	$NB4.05$
Obs. mode	2ch SDI+ADI	SDI+ADI	ADI	DI
$D_{\rm mask}$ [a] (arcsec)	0.4	0.32	0.7	no
$N_{\rm frame}(N_{\rm coadd})$	281(3)	11, 13(9)	97, 98(300)	38+38(61)
$t_{\rm frame}$ (second)	4.2	2.28	0.15	1.0
$t_{\rm total}$ [b] (minute)	53.2	8.2	146.3	77.3
$\theta_{\rm rot}$ [c] (degree)	60.6	39.0, 43.8	66.8, 67.8	18.8, 22.9
FWHM[d] (mas)	55.6	103.4	99.5	115.2
Date (yyyy-mm-dd)	2011-09-05	2011-09-13, 10-16	2012-11-21, 27	2007-12-17, 28
PI	Motohide Tamura	Michael Liu	Sascha P. Quanz	Markus Janson
Program ID	SEEDS	NICI Campaign	090.C-0777(A)	080.C-0598(A)

Notes. [(a)] Diameter of occulting mask is provided if a coronagraphic mask was used for the observation. [(b)] Total integration time ($t_{\rm total}$) is calculated from exposure time of a frame ($t_{\rm frame}$) multiplied by the number of frames ($N_{\rm frame}$) and the number of coadds ($N_{\rm coadd}$) after removal of bad frames. [(c)] Rotation angle while science frames were taken. [(d)] FWHM of the PSF is measured from unsaturated frames taken through an ND filter. For the case of NACO/Lp, average FWHM of photometric standard stars are presented.

its distinguishing speckle patterns from the parent PSF, which are roughly constant across the methane band, from true substellar companions, which exhibit a spectral dip across the methane band (Rameau et al. 2015). Although the atmospheric conditions for a substellar object to have methane in its photosphere are still under discussion, T-dwarfs with lower effective temperature, $T_{\rm eff} \leq$ 1200–1300, and higher surface gravity (assumed from their old age) tend to show methane absorption in their atmospheric spectra (e.g., Burrows et al. 1997; Janson et al. 2013; Skemer et al. 2014). The ϵ Eri b or unseen less massive companions should be fainter and older than the previously imaged planetary-mass objects, suggesting that they should have strong methane absorption in their atmospheric spectra.

Since SDI has advantages in the subtraction for fast atmospheric speckles, we performed SDI-based PSF subtraction first and then adopted ADI-based PSF subtraction, Locally Optimized Combination of Images algorithm (Lafrenière et al. 2007). For the data taken by HiCIAO and NICI, we performed the SDI-based PSF subtraction following the method applied in previous studies (e.g., Janson et al. 2007; Maire et al. 2014). This involves matching the host star PSF patterns in CH_4L to those in CH_4S. The radial positions of the speckle patterns vary proportionally with wavelength and we found the ratio to be $CH_4L/CH_4S = 1.10$ for this case. Although the host star has already been registered to the reference position, there may be residual channel-to-channel shifts because of effects such as PSF instabilities, focal plane mask misalignments, and saturation. To estimate the channel-to-channel shifts of centroids more precisely, we subtracted each frame from another frame taken simultaneously and measured the shift that minimizes a pixel-to-pixel deviation in the subtracted image.

Following the PSF subtraction, residual local noise was subtracted using the LOCI-ADI (Lafrenière et al. 2007); for the parameters N_δ, $N_{\rm A}$, g, and dr we used 0.5, 300, 1.0, and 5 (50 at outer radii of $r > 1.0''$), respectively. We also applied the PCA-ADI subtraction for residual noise (Soummer et al. 2012), and found that the result of the PCA/KLIP-ADI subtraction[3] is comparable to or a bit shallower than that of the LOCI-ADI. In this work, LOCI-ADI subtraction is employed for all datasets. As the images were obtained with ADI mode, we aligned the y-axes of each frame to celestial north and median combined to a final image. For the photometric calibration, unsaturated images of ϵ Eri taken with the neutral density filter were used. ϵ Eri was assumed to have the same average flux density per unit wavelength in the narrow-band as it does in the H-band.

3.2. Gemini-S/NICI $CH_4S + CH_4L$ narrow-band data

With SDI+ADI mode through narrow-band filters at H-band, ϵ Eri was observed by NICI at the Gemini-South telescope on 13 September and 16 October 2011, and we reduced those data archived on the Gemini Science Archive. The atmospheric conditions were poor, as inferred from the poorly corrected PSF with full width half maximum ∼103 mas. For processing, we first used the IDL-based procedure NICI_FIXWCS.pro to correct the known errors of NICI WCS, which are provided at the website of Gemini/NICI[4]. Data processing, including dark subtraction, deviant pixel correction, flat fielding, and sky subtraction, was performed as in the previous section. The F0.32 occulting mask of NICI used for the observation is an apodizing mask whose transmittance is nearly constant[5], 1/300 at 0.1−0.2″ radius from the center of the occulting spot. The PSF core was fitted with the elliptical Gaussian function and registered. The offset of position angle between channels, 1.1 degree[6], was calibrated, and then SDI-based PSF subtraction and LOCI noise subtraction were conducted similarly as described above for the HiCIAO data. The PSF of the red channel was scaled to that of the blue channel. For photometric calibration, ϵ Eri in the masked sequence was used.

3.3. VLT/NACO $L_{\rm p}$ broad-band data

With ADI mode and the Lp broad-band filter, ϵ Eri was observed by VLT/NACO on 21 and 27 November 2012 and 9 and 11 January 2013. In this work, we use only the datasets taken in 2012 because registering with high accuracy is difficult for the data taken on 9 January 2013 owing to mask misalignments. Furthermore, another dataset in 2013 was taken under

[3] We downloaded a PCA/KLIP pipeline written in IDL from http://www.astro.caltech.edu/~dmawet/pca-pipeline.html, and used those by tuning for our datasets.

[4] https://www.gemini.edu/?q=node/10237

[5] https://www.gemini.edu/sciops/instruments/nici/imaging/focal-plane-masks

[6] http://www.gemini.edu/sciops/data-and-results?q=node/10493

poor conditions inferred from worse detection sensitivities. We downloaded these unpublished archival datasets from the ESO Archive and reduced them with the LOCI-ADI procedure. PSF centering with the cross-correlation method (see Sect. 3.4) could not be used because of the large undesirable features such as a focal plane mask. Additionally, there were no unsaturated frames for registration. We therefore registered the centroids by fitting the light in the PSF outskirts to the elliptical Moffat function where the masked PSF core and regions around spider features are ignored. Images taken by NACO with ADI (pupil-tracking) mode has an offset for their position angles, which is calibrated from header information based on "ROTOFF = 179.44 – ADA.PUPILPOS" (Chauvin et al. 2012).

Since no photometric standard star was found for these data, we used the average photometric zero-point in the Lp-band, obtained between 1 November 2012 and 31 January 2013. The standard deviation of these seven zero-points was calculated to help estimate uncertainties of the photometric calibration. At least as seen in the deviation $m_{\rm zero}$, $L_{\rm p} = 22.08 \pm 0.12$, the typical variation of photometric zero-points does not significantly affect results in this work.

3.4. VLT/NACO 4.05 μm narrow-band data

We also re-analyzed the data published in Janson et al. (2008) for comparison with the newly analyzed data discussed in this paper. Data processing including dark subtraction, deviant pixel correction, sky subtraction, and flat fielding were carried out using standard procedures. For PSF centering, we registered their centroids as follows. A reference image, a middle frame among all the frames in masked sequence, is flipped and then a relative shift to the original one is estimated by cross-correlation. In fact, the image is not symmetric owing to the spider features, but the centroid is well registered thanks to stabilized patterns of diffraction rings. The frame-to-frame positional shifts were also evaluated by cross-correlation.

The images were taken at two different instrument rotator angles, with the separation being 33°. At each position, images were taken with 5–15° of sidereal rotation. Although pupil-tracking was not implemented during the observations, we conducted ADI-based PSF subtraction as follows. First, frames in each dataset were rotated to match the pupil orientation based on the header information. Median-combined frames were subtracted from the rotated frames, and then the frames were derotated to the original orientation, an approach we refer to here as "pseudo-ADI". By the pseudo-ADI method, conspicuous patterns such as spider features are subtracted, while frame-to-frame PSF subtraction is avoided, permitting a ~0.5 mag improvement in detection sensitivity at radii of 1.0–2.0″ compared with the simpler two-angle ADI and DI. The improvement becomes clearer (~1.0 mag) at an outer radius of >3.0″, thanks to the spider subtraction without the large self-subtraction effects of the ADI procedure. For photometric calibration, unsaturated frames were used.

3.5. Detection sensitivity

To estimate the detection sensitivity for the reduced images, we measured noise levels as a function of angular radii from the host star. Since neighboring pixel counts may be correlated owing to image processing steps such as centering, the reduced image was convolved with a photometric aperture ($r = FWHM$). On the convolved images, the count distribution on each radius was fitted by the Gaussian distribution, whose standard deviation is considered a 1.0σ limiting magnitude.

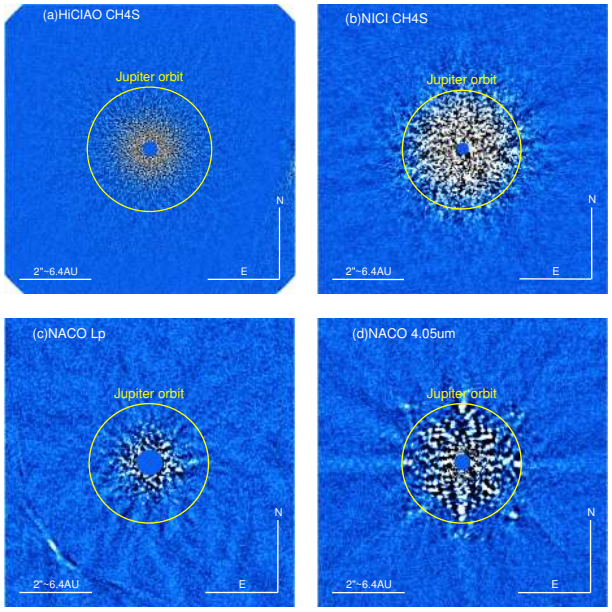

Fig. 1. Reduced images of ϵ Eri with high-contrast instruments are presented. **a)**, **b)**, **c)**, and **d)** show the image with HiCIAO/CH_4S, NICI/CH_4S, NACO/Lp, and NACO/$NB4.05$, respectively.

The LOCI algorithm can unfortunately subtract portions of true celestial sources while removing the unwanted parent star signal, the effect that is more significant at inner radii, owing to the presence of speckle noise which may resemble true point sources. To estimate the degradation level due to the effect and the self-subtraction of ADI procedure, several artificial signals generated with the Gaussian profile, whose FWHM is same as in those observations, were embedded in reduced frames before LOCI-ADI subtraction. The typical degradation factor was obtained by measuring the flux of artificial signals before and after LOCI-ADI subtraction. A correction factor was then applied to all limiting magnitudes:

$$\Delta\mathrm{mag} = m_{\rm zero} - 2.5\log\left(\frac{n\sigma(r)}{1-\psi(r)}\right) - m_{\rm primary}. \quad (1)$$

Here, n, $\sigma(r)$, and ψ(r) indicate the detection threshold, noise level, and correction factor of each radius. The attenuations in SDI-based PSF subtraction are not considered in this work. Since the unseen companion should be colder than ~500 K, around which the flux ratio in CH_4S to CH_4L is larger than 10 based on model spectra, the effect can be negligible.

4. Results and discussion

4.1. High-contrast results

The results of the observation and analysis are presented here. Figure 1 shows the reduced images of ϵ Eri taken with Subaru/HiCIAO, Gemini-S/NICI, and VLT/NACO. No significant signal of companions is detected in any of the images. The contrast curve and corresponding planetary mass detection sensitivity are presented in Fig. 2, where we employ the cooling evolutionary model, i.e., the AMES-Cond model (Allard et al. 2001; Baraffe et al. 2003). The highest contrast is achieved with Subaru/HiCIAO within 4″ (13 projected AU) from the host star. The

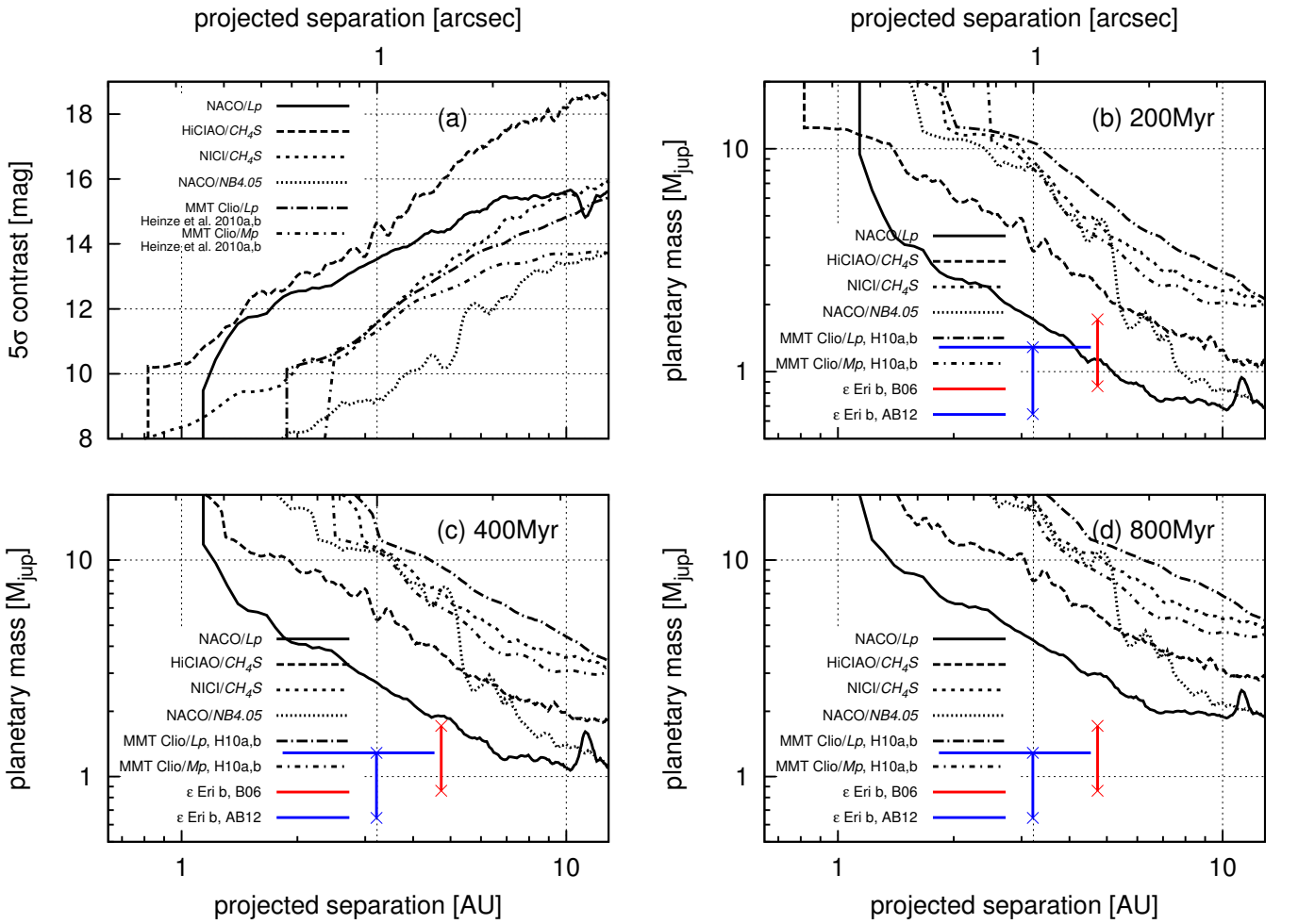

Fig. 2. Detection sensitivities of ϵ Eri. Panel **a)** shows 5σ contrast curves estimated on reduced images. For comparison, detection sensitivities with the Clio camera on the Multiple Mirror Telescope are also shown (Heinze et al. 2010a,b). Panels **b)**, **c)**, and **d)** represent 5σ detection sensitivity in terms of planetary mass based on the AMES-Cond model of 200, 400, and 800 Myr, respectively (Allard et al. 2001; Baraffe et al. 2003). The red (right) and blue (left) points in these panels show the previously reported planet, ϵ Eri b, whose projected separations are considered to be the location on 21–27 November 2012 and its possible range with known parameters (Benedict et al. 2006; Anglada-Escudé & Butler 2012), respectively. The upper and lower limit of these points correspond to the mass of ϵ Eri b with $\sin i = 0.5$ and 1.0, respectively.

combination of SDI and ADI (LOCI) works well for PSF subtraction if the companions have clear spectral differences across these two narrow-band filters. In such instances, SDI not only allows an effective PSF subtraction, but also reduces LOCI's unwanted degradation of point source companions thanks to the simultaneous speckle subtraction before LOCI.

To understand the sensitivity in terms of planetary mass, we employed a cooling evolutionary model, AMES-Cond model (Allard et al. 2001; Baraffe et al. 2003). There are several cooling evolutionary models, mainly categorized as Dusty for L-dwarfs and Dust-Free for T-dwarfs (e.g., Chabrier et al. 2000; Baraffe et al. 2003). In this work, we search for T-type (or less massive) companions around the star, and our detection sensitivities achieve deeper than the upper limit of T-dwarfs range, $T_{\rm eff}$ = 1200–1300 K. Furthermore less massive planets, 1.0−2.0 $M_{\rm jup}$, have a lower effective temperature, <1000 K, even at a very early stage of their evolution (Baraffe et al. 2003). We therefore employ a Dust-Free model, i.e., the AMES-Cond model for our analysis.

Since the magnitudes of the young substellar objects in narrow-band filters used here are not listed in Baraffe et al. (2003), we adopt the 200–1000 K model spectra used in their models as unseen objects around ϵ Eri. Using the model spectra and the filter response curves for the respective instruments, the predicted colors of young stellar objects were obtained for a 200 K (or 1000 K) surface temperature: $CH_4S - H$ = −0.61(−0.14) for HiCIAO, $CH_4S - H$ = −0.50(−0.61) for NICI, and $NB4.05 - L_{\rm p}$ = −2.12(−0.63) for NACO, and were applied to all limiting magnitudes of narrow-band filters. It also should be noted that this color correction for narrow-band filters is extremely dependent on atmospheric models: dust cloud, surface gravity, and metallicity. If recent model spectra are used for the color correction (Morley et al. 2012, 2014), predicted colors can also be obtained for a 200 K (or 1000 K) object: $CH_4S - H$ = −0.64(−0.02) for HiCIAO, $CH_4S - H$ = −1.53(−0.33) for NICI, and $NB4.05 - L_{\rm p}$ = −1.23(−0.93) for NACO.

Since substellar objects emit a large fraction of their light at longer wavelengths, 3–5 μm (e.g., Skemer et al. 2014), the deepest sensitivity in terms of planetary mass is achieved in the Lp-band even though the highest contrast is achieved at shorter wavelengths. Our results presented here also suggest that the nearly diffraction-limited PSF in the Lp-band is more effective for planet searches than the modest PSF (SR = 0.3–0.4) in the H-band based on the AMES-Cond model, even at small radii ($r > 0.3''$). Although the Lp-band likely achieves greater sensitivity for low-mass companions based on the AMES-Cond

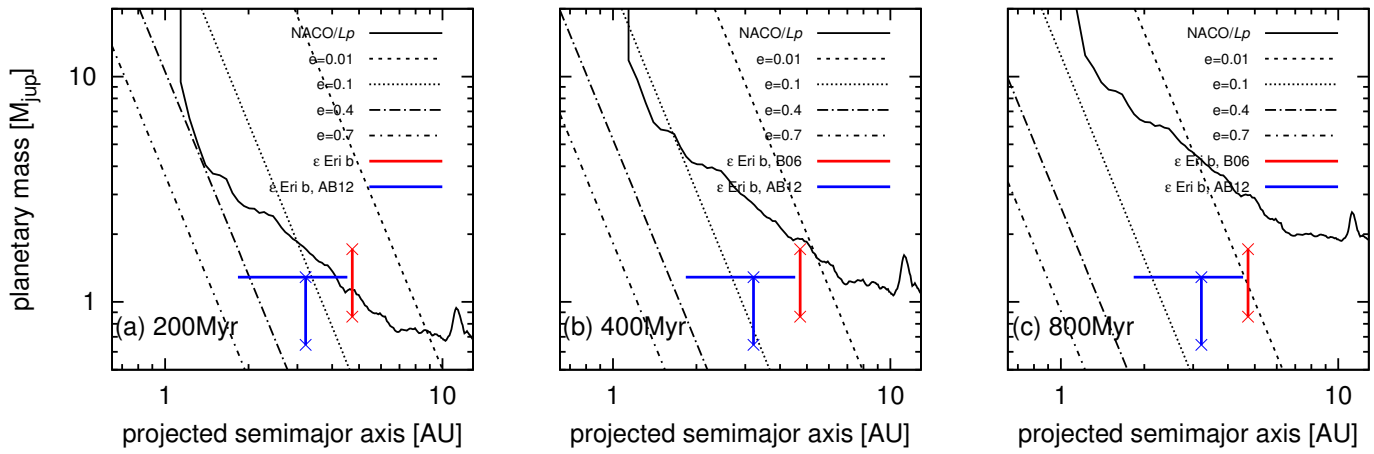

Fig. 3. Detection sensitivity of ϵ Eri obtained by NACO/L_P as a solid curve and ϵ Eri b are plotted as in Fig. 2, based on the AMES-Cond model with ages of 200, 400, and 800 Myr *from left to right*. The contours of the secular perturbation are shown for the asymmetric disk with different orbital eccentricities where $t_{\rm cross} = t_{\rm age}$ is assumed. Dotted and dashed curves represent contours corresponding to the different orbital eccentricities of a planet around ϵ Eri: 0.01, 0.1, 0.4, and 0.7.

model, the costs of observing time should be considered because the integration time of the Lp dataset is about three times longer than that of H-band narrow-band filters.

4.2. Expected position of ϵ Eri b

If 200 Myr of the AMES-Cond model is assumed, then the deepest detection sensitivity in this work is comparable to the mass of ϵ Eri b reported from radial velocity investigations (Fig. 2). To estimate our detection probabilities for ϵ Eri b, we consider the position of the companion when L_P-band imaging observations were conducted. There are two different parameter sets proposed for the orbit of ϵ Eri b: Benedict et al. (2006) and Anglada-Escudé & Butler (2012). In the case of Benedict et al. (2006), ϵ Eri b should have been at a separation of ∼1.47″, with a position angle of ∼133°, on 21–27 November 2012. Hence, the companion should have been detected with $L_{\rm p}$ imaging observations if the age of the system is 200 Myr or younger. On the other hand, since the inclination angle is not determined in Anglada-Escudé & Butler (2012), we assume here that the orbital plane of ϵ Eri b is aligned with the dust disk, which is one of the most likely assumptions because there are no clear reasons to misalign the inclination angle of the planet and the disk, for instance an additional massive companion for the Kozai mechanism (Kozai 1962). Based on this assumption, we conclude that the planet cannot be detected with 5σ significance in our observations, if 200 Myr is adopted as the age of the system. Our imaging results therefore marginally reject the case of 200 Myr as the system age of ϵ Eri, and older ages are preferable. However, it should be noted that the cooling evolutionary model has uncertainties, molecular opacities for instance. In addition, the presence of ϵ Eri b and its orbital parameters are still to be refined, a step that requires observational calibrations for the cooling evolutionary model and more precise orbital characterization for the system.

4.3. Constraint on the ϵEri planetary system

Previous studies of ϵ Eri have reported the presence of an asymmetric dust disk and a massive planet with large orbital eccentricity. To explain the asymmetric morphology, the presence of an embedded planet, 0.1 $M_{\rm jup}$ at 40 AU, has been suggested (e.g., Quillen & Thorndike 2002; Deller & Maddison 2005). Asteroids are locked into mean motion resonances with the planet, enhancing the asymmetricity and dust replenishment. Future observations with next-generation high-contrast instruments should be able to verify the unseen planet.

An alternative explanation for the dust replenishment of the disk is a secular perturbation by ϵ Eri b that is radially distant from the disk (Mustill & Wyatt 2009). For this alternative scenario, perturbations for asteroids with 80 m–100 km radii have been considered. The presence of asteroids with this size has been observationally indicated in Greaves et al. (2014). The timescale of the secular perturbation, $t_{\rm cross}$, is obtained with Eq. (2) (see below). It can be considered that a giant planet with non-zero eccentricity induces the collision of asteroids if the required timescale given in Eq. (2) is shorter than the system age, $t_{\rm age}$:

$$t_{\rm cross} \sim 1.46 \frac{(1-{e_{\rm pl}}^2)^{3/2}}{e_{\rm pl}} \left(\frac{a_{\rm disk}}{10\ {\rm AU}}\right)^{9/2} \times \left(\frac{M_{\rm s}}{M_\odot}\right)^{1/2} \left(\frac{M_{\rm pl}}{M_{\rm jup}}\right)^{-1} \left(\frac{a_{\rm pl}}{1\ {\rm AU}}\right)^{-3}\ {\rm yr}. \quad (2)$$

In the above equation, the orbital eccentricity of a massive planet, disk location in radial distance from the host star, mass of the host star, mass of the planet, and semimajor axis of the planet are given by $e_{\rm pl}, a_{\rm disk}, M_{\rm s}, M_{\rm pl}$, and $a_{\rm pl}$, respectively. For $a_{\rm disk}, M_{\rm s}$, and $a_{\rm pl}$, we used 17.7″ (57 AU), 0.83 $M_\odot$, and 3.39 AU, respectively (Benedict et al. 2006; Lestrade & Thilliez 2015). Here we assume that ϵ Eri b is a single perturbation source for the dust disk. Figure 3 presents the detection sensitivity obtained in this work, the contours of the secular perturbation, and the constraints on ϵ Eri b. In the case of a 400 Myr system, our results suggest that a giant planet within 5 AU has a non-circular orbit. The specific required eccentricity for ϵ Eri b is over ∼0.015 and 0.06 for Benedict et al. (2006) and Anglada-Escudé & Butler (2012), which is consistent with the RV results, 0.7 and 0.4, respectively. To explain the large orbital eccentricity of ϵ Eri b, the presence of other lower mass planets is preferred. Since ϵ Eri is an isolated star, as confirmed by deep wide-field-of-view imaging with the *Spitzer* space telescope (Janson et al. 2015), and since the inclination angle of the dust disk and ϵ Eri b are aligned, secular perturbations due to an

additional companion producing a Kozai mechanism cannot be considered as the origin of the giant planet's high eccentricity.

5. Conclusions

We report the results of high-contrast imaging for ϵ Eri. The deeper sensitivities in the Lp-band and CH_4S within the H-band are reported in this work. The achieved contrasts are 13.5 and 14.7 mag at 1.0″ in Lp and CH_4S, respectively. Our results suggest that observations with the Lp-band can achieve deeper sensitivity in planetary mass than the shorter wavelength narrow-band filters for detecting lower mass companions based on a cooling evolutionary model, if sufficient time (about half a night) can be used for a target. The origin of the replenished dust disk is also discussed. The peculiar morphology of the dust disk and the large eccentricity of ϵ Eri b strongly suggest that ϵ Eri is a planetary system with multiple planets, even if ϵ Eri b is assumed as a single perturbation source for the disk. To have a precise understanding of this system, the next observational approaches should be the deep imaging for the scattered light from less massive planets, and high dispersion spectroscopy in the near-infrared wavelengths for more precise RV measurements. Astrometry also has an important role in orbital characterizations of the RV-discovered planet, ϵ Eri b, that can induce a relatively large stellar wobble, up to 1.3–1.5 mas from the barycenter of the system. Unfortunately, ϵ Eri is too bright for *Gaia*'s nominal mission, and so a specified program or a smaller space telescope for astrometry is required.

Acknowledgements. The authors thank the anonymous referee for useful comments, the Subaru Telescope staff for their assistance, David Lafreniere for generously providing the source code for the LOCI algorithm, and also Dimitri Mawet and his collaborators for providing the source code for the PCA/KLIP algorithm in their website. This work was conducted based on: (a) data collected at Subaru Telescope, which is operated by the National Astronomical Observatory of Japan, especially "Strategic Exploration of Exoplanets and Disks with Subaru"; (b) observations obtained at the Gemini Observatory acquired through the Gemini Science Archive, which is operated by the Association of Universities for Research in Astronomy, Inc., under a cooperative agreement with the NSF on behalf of the Gemini partnership: the National Science Foundation (United States), the National Research Council (Canada), CONICYT (Chile), Ministerio de Ciencia, Tecnología e Innovación Productiva (Argentina), and Ministério da Ciência, Tecnologia e Inovação (Brazil); and (c) data obtained from the ESO Science Archive Facility under request number 175360 SAF and 191119 SAF. T.M. is supported by the Program for Leading Graduate Schools, "Inter-Graduate School Doctoral Degree Program on Global Safety", by the Ministry of Education, Culture, Sports, Science, and Technology. J.C. is supported by the US National Science Foundation under Award No. 1009203. M.K. was supported by Japan Society for Promotion of Science (JSPS) Fellowship for Research, and this work was partially supported by the Grant-in-Aid for JSPS Fellows (Grant Number 25-8826). The authors wish to recognize and acknowledge the very significant cultural role and reverence that the summit of Mauna Kea has always had within the indigenous Hawaiian community. We are most fortunate to have the opportunity to conduct observations from this mountain.

References

Allard, F., Hauschildt, P. H., Alexander, D. R., Tamanai, A., & Schweitzer, A. 2001, ApJ, 556, 357
Anglada-Escudé, G., & Butler, R. P. 2012, ApJS, 200, 15
Baraffe, I., Chabrier, G., Barman, T. S., Allard, F., & Hauschildt, P. H. 2003, A&A, 402, 701
Benedict, G. F., McArthur, B. E., Gatewood, G., et al. 2006, AJ, 132, 2206
Burgasser, A. J., Geballe, T. R., Leggett, S. K., Kirkpatrick, J. D., & Golimowski, D. A. 2006, ApJ, 637, 1067
Burrows, A., Marley, M., Hubbard, W. B., et al. 1997, ApJ, 491, 856
Chabrier, G., Baraffe, I., Allard, F., & Hauschildt, P. 2000, ApJ, 542, 464
Chauvin, G., Lagrange, A.-M., Beust, H., et al. 2012, A&A, 542, A41
Cutri, R. M., Skrutskie, M. F., van Dyk, S., et al. 2003, 2MASS All Sky Catalog of point sources
Deller, A. T., & Maddison, S. T. 2005, ApJ, 625, 398
Fuhrmann, K. 2004, Astron. Nachr., 325, 3
Gray, R. O., Corbally, C. J., Garrison, R. F., et al. 2006, AJ, 132, 161
Greaves, J. S., Holland, W. S., Moriarty-Schieven, G., et al. 1998, ApJ, 506, L133
Greaves, J. S., Holland, W. S., Wyatt, M. C., et al. 2005, ApJ, 619, L187
Greaves, J. S., Sibthorpe, B., Acke, B., et al. 2014, ApJ, 791, L11
Hatzes, A. P., Cochran, W. D., McArthur, B., et al. 2000, ApJ, 544, L145
Heinze, A. N., Hinz, P. M., Kenworthy, M., et al. 2010a, ApJ, 714, 1570
Heinze, A. N., Hinz, P. M., Sivanandam, S., et al. 2010b, ApJ, 714, 1551
Hoeg, E., Bässgen, G., Bastian, U., et al. 1997, A&A, 323, L57
Høg, E., Fabricius, C., Makarov, V. V., et al. 2000, A&A, 355, L27
Ida, S., & Lin, D. N. C. 2004, ApJ, 604, 388
Ida, S., Lin, D. N. C., & Nagasawa, M. 2013, ApJ, 775, 42
Janson, M., Brandner, W., Henning, T., et al. 2007, AJ, 133, 2442
Janson, M., Reffert, S., Brandner, W., et al. 2008, A&A, 488, 771
Janson, M., Brandt, T. D., Kuzuhara, M., et al. 2013, ApJ, 778, L4
Janson, M., Quanz, S. P., Carson, J. C., et al. 2015, A&A, 574, A120
Kozai, Y. 1962, AJ, 67, 591
Lafrenière, D., Marois, C., Doyon, R., Nadeau, D., & Artigau, É. 2007, ApJ, 660, 770
Lestrade, J.-F., & Thilliez, E. 2015, A&A, 576, A72
Maire, A.-L., Boccaletti, A., Rameau, J., et al. 2014, A&A, 566, A126
Mamajek, E. E., & Hillenbrand, L. A. 2008, ApJ, 687, 1264
Marois, C., Lafrenière, D., Doyon, R., Macintosh, B., & Nadeau, D. 2006, ApJ, 641, 556
Mayor, M., & Queloz, D. 1995, Nature, 378, 355
Morley, C. V., Fortney, J. J., Marley, M. S., et al. 2012, ApJ, 756, 172
Morley, C. V., Marley, M. S., Fortney, J. J., et al. 2014, ApJ, 787, 78
Mustill, A. J., & Wyatt, M. C. 2009, MNRAS, 399, 1403
Pollack, J. B., Hubickyj, O., Bodenheimer, P., et al. 1996, Icarus, 124, 62
Quillen, A. C., & Thorndike, S. 2002, ApJ, 578, L149
Racine, R., Walker, G. A. H., Nadeau, D., Doyon, R., & Marois, C. 1999, PASP, 111, 587
Rameau, J., Chauvin, G., Lagrange, A.-M., et al. 2015, A&A, 581, A80
Skemer, A. J., Marley, M. S., Hinz, P. M., et al. 2014, ApJ, 792, 17
Soummer, R., Pueyo, L., & Larkin, J. 2012, ApJ, 755, L28
Suzuki, R., Kudo, T., Hashimoto, J., et al. 2010, in SPIE Conf. Ser., 7735, 30
Tamura, M. 2009, in AIP Conf. Ser. 1158, eds. T. Usuda, M. Tamura, & M. Ishii, 11
van Leeuwen, F. 2007, A&A, 474, 653
Wu, Y., & Murray, N. 2003, ApJ, 589, 605
Wyatt, M. C. 2008, ARA&A, 46, 339
Zechmeister, M., Kürster, M., Endl, M., et al. 2013, A&A, 552, A78

[1] Astronomical Institute, Tohoku University, Aoba-ku, Sendai, 980-8578 Miyagi, Japan
e-mail: mizuki@astr.tohoku.ac.jp
[2] Institute of Space and Astronautical Science, JAXA, 3-1-1 Yoshinodai, Sagamihara, Kanagawa Japan
[3] Department of Physics and Astronomy, College of Charleston, 58 Coming St., Charleston, SC 29424, USA
[4] Department of Earth and Planetary Sciences, Tokyo Institute of Technology, 2-12-1 Ookayama, Meguro-ku, 152-8551 Tokyo, Japan
[5] Astrobiology Center of NINS, 2-21-1, Osawa, Mitaka, 181-8588 Tokyo, Japan
[6] National Astronomical Observatory of Japan, 2-21-1, Osawa, Mitaka, 181-8588 Tokyo, Japan
[7] Department of Physics, University of Cincinnati, Cincinnati, OH 45221-0011, USA
[8] Subaru Telescope, National Astronomical Observatory of Japan, 650 North A'ohoku Place, Hilo, HI96720, USA
[9] Laboratoire Lagrange (UMR 7293), Université de Nice-Sophia Antipolis, CNRS, Observatoire de la Côte d'Azur, 28 avenue Valrose, 06108 Nice Cedex 2, France
[10] Max Planck Institute for Astronomy, Königstuhl 17, 69117 Heidelberg, Germany
[11] Astrophysics Department, Institute for Advanced Study, Princeton, NJ 08540, USA
[12] Universitäts-Sternwarte München, Ludwig-Maximilians-Universität, Scheinerstr. 1, 81679 München, Germany
[13] Exoplanets and Stellar Astrophysics Laboratory, Code 667, Goddard Space Flight Center, Greenbelt, MD 20771, USA

[14] Eureka Scientific, 2452 Delmer, Suite 100, Oakland CA96002, USA
[15] Goddard Center for Astrobiology, USA
[16] Institute for Astronomy, University of Hawaii, 640 N. A'ohoku Place, Hilo, HI 96720, USA
[17] Department of Astrophysical Science, Princeton University, Peyton Hall, Ivy Lane, Princeton, NJ08544, USA
[18] Department of Astronomy, The University of Tokyo, 7-3-1, Hongo, Bunkyo-ku, 113-0033 Tokyo, Japan
[19] Department of Earth and Space Science, Graduate School of Science, Osaka University, 1-1 Machikaneyamacho, Toyonaka, 560-0043 Osaka, Japan
[20] Hiroshima University, 1-3-2, Kagamiyama, Higashihiroshima, 739-8511 Hiroshima, Japan
[21] Department of Astrophysics, CAB-CSIC/INTA, 28850 Torrej'on de Ardoz, Madrid, Spain
[22] Jet Propulsion Laboratory, California Institute of Technology, Pasadena, CA, 171-113, USA
[23] Department of Astronomical Science, The Graduate University for Advanced Studies, 2-21-1, Osawa, Mitaka, 181-8588 Tokyo, Japan
[24] Institute of Astronomy and Astrophysics, Academia Sinica, PO Box 23-141, 10617 Taipei, Taiwan
[25] Swiss Federal Institute of Technology (ETH Zurich), Institute for Astronomy, Wolfgang-Pauli-Strasse 27, 8093 Zurich, Switzerland
[26] Kavli Institute for Physics and Mathematics of the Universe, The University of Tokyo, 5-1-5, Kashiwanoha, Kashiwa, 277-8568 Chiba, Japan
[27] Department of Cosmosciences, Hokkaido University, Kita-ku, Sapporo, 060-0810 Hokkaido, Japan
[28] H. L. Dodge Department of Physics and Astronomy, University of Oklahoma, 440 WBrooks St Norman, OK 73019, USA